Advanced Functional Materials

ADVANCED FUNCTIONAL MATERIALS
www.afm-journal.de

RESEARCH ARTICLE

Cu-Induced Self-Adaptive Crystallization and Interfacial Stabilization in Cr_2AlC Coatings for Advanced Electrical Contact Applications

Yiqun Feng[1] | Qizhen He[1] | Guanshui Ma[1] | Zhenyu Wang[1] | Peiling Ke[1,2] | Aiying Wang[1,2]

[1]State Key Laboratory of Advanced Marine Materials, Zhejiang Key Laboratory of Extreme-environmental Material Surfaces and Interfaces, Ningbo Institute of Materials Technology and Engineering, Chinese Academy of Sciences, Ningbo, China | [2]Center of Materials Science and Optoelectronics Engineering, University of Chinese Academy of Sciences, Beijing, China

Correspondence: Zhenyu Wang (wangzy@nimte.ac.cn) | Aiying Wang (aywang@nimte.ac.cn)

Received: 4 March 2026 | **Revised:** 7 August 2026 | **Accepted:** 1 September 2026

Keywords: Cr_2AlC MAX phase coatings | Cu doping | current-carrying wear | electrical contact materials | self-adaptive crystallization

ABSTRACT

Electrical contact materials for advanced power transmission and electromagnetic systems must simultaneously provide high electrical conductivity, arc-erosion resistance, and tribological stability under extreme electro-thermo-mechanical conditions. Herein, Cr_2AlC and Cu-doped Cr_2AlC (Cr_2AlC-Cu) coatings were deposited on 7075 aluminum alloy via hybrid arc-magnetron sputtering followed by low-temperature annealing at 400°C. With increasing Cu content (0-9.1 at.%), the coating microstructure evolves from single-phase Cr_2AlC to a dual-phase architecture consisting of Cr_2AlC and Al_4Cu_9. All coatings exhibit high hardness values (18.8-21.2 GPa), originating from grain refinement and amorphous-nanocrystalline structures induced by low-temperature annealing. The Cu-rich coating demonstrates the lowest electrical resistivity (119 μΩ·cm) and superior resistance to arc erosion. This performance enhancement is attributed to Cu-assisted Al-Cu interdiffusion, which accelerates in situ MAX-phase crystallization and promotes the formation of conductive interfacial networks under Joule heating, establishing a positive feedback mechanism that stabilizes electrical transport and suppresses arc erosion. Moreover, the formation of an adherent Cu transfer layer transforms the frictional interface into a Cu-Cu sliding contact, effectively reducing friction and preventing adhesive wear of the aluminum substrate. These synergistic effects activate a self-adaptive crystallization and lubrication mechanism during service, highlighting Cu-doped Cr_2AlC coatings as promising candidates for next-generation electrical contact applications.

1 | Introduction

Electrical contact materials are essential components of power transmission systems, where they must simultaneously provide high electrical conductivity, wear resistance, and thermal stability. The interplay of current flow, friction, and elevated temperatures makes their tribological behavior highly complex, directly influencing the precision, reliability, and service life of the entire electrical contact system [1–4]. With the rapid advancement of high-speed maglev transportation, aerospace propulsion, and electromagnetic launching technologies, these materials are increasingly exposed to extreme service conditions characterized by strong electro-magneto-thermo-mechanical coupling, including high current density, ultrahigh velocity, severe temperature rise, and intense mechanical strain [5–7]. Under such conditions, the ideal electrical contact material must not only ensure

[Correction added on September 10, 2026, after first online publication: Couple of typo errors have been corrected in this version.]

excellent electrical conductivity but also exhibit outstanding resistance to arc erosion, mechanical wear, and molten metal attack.

Aluminum and copper alloys have attracted attention as candidate materials for electromagnetic rail launchers, serving as armature and rail components due to their low density and high conductivity, respectively [8, 9]. However, during operation, the aluminum armature often undergoes surface melting, leading to the transfer of adherent aluminum layers onto the copper rail. This interfacial adhesion results in severe gouging, arc discharge, and catastrophic wear, ultimately compromising system lifetime and reliability [10, 11]. To mitigate these challenges, research has generally pursued two strategies: (i) the development of novel bulk alloys or surface-modified copper rails [12, 13], and (ii) the application of protective coatings on aluminum armatures to suppress molten aluminum adhesion and stabilize the electrical contact interface [14, 15].

A variety of coating systems for aluminum armatures have been explored, yet each exhibits inherent limitations. Pure Cu coatings [16] suffer from poor adhesion; low-melting-point metal coatings such as Sn, In, and Bi [17] reduce friction through liquefaction but lead to unstable contact resistance; solid-lubricant coatings such as PTFE-MoS_2 composites [18] provide anti-adhesion effects but face issues of thermal expansion mismatch and weak bonding; while carbon-nanotube-doped coatings [19] suppress aluminum splashing yet lack adequate high-temperature stability and electrical conductivity. This body of work underscores the urgent need for a new coating paradigm that integrates high electrical conductivity, robust thermal stability, and adaptive lubricating behavior under extreme operating conditions.

MAX phase coatings have attracted considerable attention as promising conductive, wear-resistant materials owing to their unique layered crystal structure. Belonging to a class of layered ceramics with the general formula $M_{n+1}AX_n$ (where M is an early transition metal, A is an A-group element, and X is carbon or nitrogen), these materials integrate metallic and ceramic characteristics within a single phase. Their bonding structure combines metallic, covalent, and ionic interactions, which endows them with high strength and toughness alongside excellent electrical and thermal conductivity. As a result, MAX phases exhibit superior oxidation resistance, remarkable thermal shock tolerance, and structural stability under rapid thermal cycling. These combined properties make them highly attractive for applications in aerospace, energy systems, and chemical processing, where both conductivity and durability under extreme conditions are required [20–22].

Cr_2AlC has emerged as a promising candidate for electrical contact applications owing to its high electrical conductivity, excellent corrosion resistance, and superior oxidation resistance [23–26]. Reuban et al. [27] reported that at elevated temperatures, Cr_2AlC decomposes into Cr_7C_3, forming multiphase grain boundaries on the material surface. These boundaries act as diffusion channels for aluminum, thereby promoting the rapid formation of a dense Al_2O_3 passivation layer, which is widely recognized as the key mechanism underlying the outstanding oxidation resistance of Cr_2AlC.

In recent years, increasing attention has been devoted to developing composite materials that integrate the mechanical advantages of MAX phases with the electrical conductivity of Cu- or Ag-based systems. Ngai et al. [28] demonstrated that doping Cu with Ti_3SiC_2 enhances both density and mechanical properties without significantly degrading electrical conductivity, resulting in superior arc-erosion resistance. Similarly, Yang et al. [29] fabricated Cu/Ti_3SiC_2 composites and found that the addition of Cu substantially improved the flexural strength, electrical conductivity, and wear resistance of Ti_3SiC_2, thereby broadening its potential applications in rail transportation and other fields. However, relevant composite coatings have rarely been reported.

A materials design strategy based on a Cr_2AlC-Cu nanocomposite coating system is proposed. This approach employs the ternary layered MAX-phase ceramic Cr_2AlC as the structural matrix, synergistically integrated with Cu as a functional dopant. Four key factors provide the rationale for this approach. First, favorable atomic size matching between Cr (1.27 Å), Al (1.43 Å), and Cu (1.28 Å), combined with strong orbital hybridization between Cu 3d and Cr/Al d orbitals, enhances interfacial cohesion and electronic continuity [30, 31]. Second, Cu is introduced to enhance the electrical conductivity of the coating, owing to its intrinsically high electrical conductivity [32]. Third, trace Cu doping refines grains [33] and strengthens the coating [34, 35], which enhances hardness and toughness. Finally, Cu provides an intrinsic solid-lubricating effect [36], diffusing to the surface during frictional and Joule heating to form a lubricating transfer film that mitigates wear and suppresses adhesive transfer.

Guided by these design principles, Cr_2AlC coatings with varying Cu contents were fabricated on 7075 aluminum alloy substrates using a hybrid arc and DC magnetron sputtering process, followed by vacuum annealing at 400°C for 24 h. The effects of Cu incorporation on coating resistivity, mechanical properties, and performance under current-carrying friction and arc ablation were systematically evaluated. The results reveal a previously unreported mechanism: Cu incorporation facilitates Al diffusion within the coating, which promotes the crystallization of the Cr_2AlC MAX phase during post-deposition annealing. During electrical contact testing, the Cu-containing coating maintains a stable Cr_2AlC structure due to reduced Joule heating. Meanwhile, Cu-rich transfer layers formed on the coating surface and Al diffusion pathways at the interface contribute to the establishment of stable metallic conductive networks during current-carrying friction. This Cu-induced self-adaptive behavior enables sustained electrical conductivity and improved interfacial stability under current-carrying conditions.

2 | Results

2.1 | Microstructure, Composition and Phase Structure of the Coatings

Unless otherwise specified, all samples discussed and analyzed in the following sections are the coatings subjected to post-deposition annealing at 400°C. Figure 1a shows the schematic diagram of coating preparation and low-temperature vacuum treatment. By varying the sputtering targets, three series of

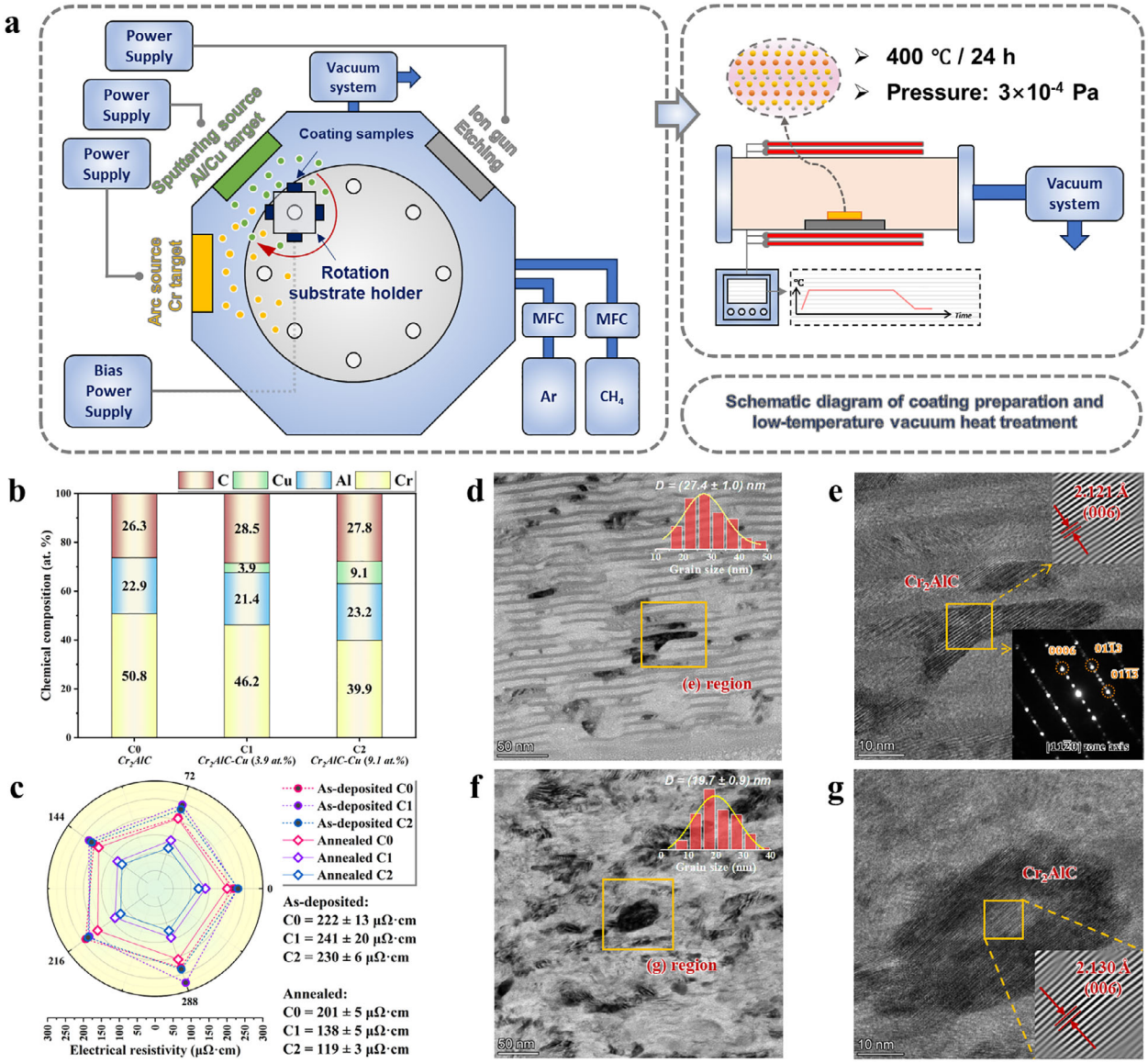

FIGURE 1 | (a) Schematic of hybrid cathodic arc/magnetron and annealing treatment process. (b) Chemical compositions and (c) electrical resistivity of all coatings. (d) Bright-field image of the C0 coating. (e) Enlarged image of (d) with FFT pattern of the yellow-marked region and corresponding SAED pattern. (f) Bright-field image of the C2 coating. (g) Enlarged image of (f) with FFT pattern.

Cr_2AlC-Cu coatings were prepared in this study, designated as C0, C1, and C2. The sample designation was based on the copper content in the Cr_2AlC-Cu coatings, where C denotes copper. The digits 0, 1, and 2 correspond to the copper content in the sputtering target: C0 represents a pure aluminum target, C1 corresponds to an Al-Cu target with a 90:10 atomic ratio, and C2 corresponds to an Al-Cu target with an 80:20 atomic ratio. In summary, C0 represents Cr_2AlC coatings, while C1 and C2 are Cr_2AlC-Cu coatings with different copper contents.

Figure 1b shows the chemical compositions of all coatings, where the copper contents of C1 and C2 were measured to be 3.9 and 9.1 at.%, respectively. The cross-sectional images of all coatings are shown in Figure S1. All specimens exhibit a dense structure without cracks or obvious defects at the coating-substrate interface, indicating excellent adhesion. The coating thickness ranges from 7.53 to 8.58 μm and increases slightly with higher copper content. The measured surface roughness values were 7.2 ± 0.3, 7.6 ± 0.4, and 7.1 ± 0.5 nm for C0, C1, and C2, respectively.

Figure 1c presents the electrical resistivity of all coatings. Four-point probe measurements were performed on each sample at five rotation angles, and the results for both as-deposited and annealed coatings are reported. The averaged values, also reported in Figure 1c, indicate that the resistivity of each coating decreased after 24 h of heat treatment at 400°C. Among them, the annealed C2 coating exhibited the lowest electrical resistivity (~119 μΩ·cm), which is lower than that of the C0 coating (~201 μΩ·cm) and the C1 coating (~138 μΩ·cm). These results demonstrate that the electrical resistivity of the annealed coatings decreases with increasing copper content. In other words, the addition of Cu contributes to optimizing the conductivity of the coatings after heat treatment.

Figure 1d,e presents the TEM bright-field images of C0 coatings, revealing a distinct multilayer structure that consists of crystalline and amorphous phases. The corresponding EDS mapping (Figure S2a) reveals that the multilayer structure was separated into Cr-rich and Al-rich regions, and the crystalline regions corresponding to the Al-rich zones. The selected area electron diffraction (SAED) pattern of C0 (Figure S2b) displays concentric diffraction rings and a central amorphous ring, which match the interplanar spacings of the Cr_2AlC MAX phase. Fast Fourier transform (FFT) analysis of Figure 1e further confirms the presence of the (006) plane with a spacing of 0.214 nm, characteristic of the Cr_2AlC MAX phase. The crystalline grains, elongated due to the layered structure, range from 10 to 50 nm with an average size of approximately 27.4 nm (Figure 1d).

For C1 (Figure S2c), TEM and EDS reveal the presence of copper in the form of clusters. Although the Cr-Al multilayer structure remains, its continuity is partially disrupted. Bright-field imaging (Figure S2d) and SAED patterns (Figure S2e) confirm the crystalline Cr_2AlC MAX phase. Grain size analysis (Figure S2f) indicates an average size of around 11.8 nm, showing that copper addition promotes grain refinement compared with C0.

Figure 1f,g show TEM analysis of C2 coatings; the HAADF-TEM image and EDS mapping (Figure S2g) reveal significant disruption of the multilayer structure due to higher copper content. Bright-field images (Figure 1g; Figure S2i) show Cu-free and Cu-rich regions. In the Cu-rich region (Figure S2i), FFT analysis yields an interplanar spacing of 0.195 nm, corresponding to the (420) plane of Al_4Cu_9. SAED patterns (Figure S2j) confirm the cubic Al_4Cu_9 phase along the [111] zone axis, with planes $(10\bar{1})$, $(1\bar{1}0)$ and $(0\bar{1}1)$ clearly identified. In addition, Cr_2AlC MAX phase is also observed in C2, as evidenced by the FFT (Figure 1g) and SAED (Figure S2k). Figure S2l displays distinct diffraction rings corresponding to nanocrystalline Cr_2AlC (yellow lines) and Al_4Cu_9 (red lines). The average grain size is about 19.7 ± 0.9 nm (Figure 1f), larger than C1 but smaller than C0.

The XRD patterns of all coatings are presented in Figure 2a. All specimens exhibit diffraction peaks characteristic of the Cr_2AlC MAX phase. The peaks at approximately 13.6°, 27.4°, 41.9°, 56.8°, 65.4°, 76.5°, and 80.8° can be attributed to the (002), (004), (103), (106), (110), (109), and (116) planes of Cr_2AlC, respectively (ICDD#01-089-2275). For the C1 and C2 coatings, an additional Al_4Cu_9 phase was identified at $2\theta = 43.8°$, indicating the evolution from a predominantly single Cr_2AlC MAX-phase structure to a dual-phase structure consisting of Cr_2AlC and Al_4Cu_9 intermetallic phases with increasing Cu content. The relatively weak signal-to-noise ratio of XRD indicates limited crystallization of the MAX phase. Raman spectroscopy was further employed to confirm the phase composition (Figure S3). After eliminating matrix interference, two Raman peaks were observed at 246.0 and 334.8 cm^{-1}, corresponding to the characteristic modes of the Cr_2AlC MAX phase, consistent with previous reports. Together, XRD and Raman results confirm the successful synthesis of the Cr_2AlC phase in the coating.

While conventional θ-2θ XRD confirms the Cu-induced change in phase constitution from a predominantly Cr_2AlC-based structure to a dual-phase structure consisting of Cr_2AlC and Al_4Cu_9 intermetallic phases, its projection nature precludes a reliable assessment of crystallographic texture and interphase orientation relationships. To resolve the 3D grain orientation distribution and to determine whether the Al_4Cu_9 phase develops a preferred or epitaxial alignment with the MAX matrix, X-ray pole figure analysis was employed, providing critical insight into the texture-driven architecture of the composite coating.

Pole-figure measurements reveal a clear and reproducible orientation correlation between the Cr_2AlC MAX phase and the Al_4Cu_9 intermetallic phase in Cu-containing coatings. For the low-Cu sample (3.9 at.% Cu), the Cr_2AlC (002) pole is located close to the center of the pole figure ($\chi \approx 2.5°$, $\varphi \approx 95°$), while the Al_4Cu_9 (330) pole appears at the exact center position ($\chi = 0°$, $\varphi = 0°$). The near coincidence of these two poles indicates that the corresponding plane normals are nearly collinear.

In the high-Cu sample (9.1 at.% Cu), the Al_4Cu_9 (330) pole remains centered ($\chi = 0°$, $\varphi = 0°$), whereas the dominant Cr_2AlC pole shifts to the (103) reflection, which is located at $\chi \approx 7.5°$ and $\varphi \approx 250°$. Despite the change in the dominant MAX-phase reflection, the spatial proximity between the Cr_2AlC and Al_4Cu_9 poles is preserved, indicating a consistent axial alignment between the two phases.

The measured pole-figure peak positions (χ, φ) were converted into Cartesian unit vectors, and the angular separation θ between the MAX-phase poles and the Al_4Cu_9 (330) pole was calculated. For the low-Cu sample, the angular separation between the Cr_2AlC (002) pole and the Al_4Cu_9 (330) pole is 2.5°. For the high-Cu sample, the corresponding angular separation between the Cr_2AlC (103) pole and the Al_4Cu_9 (330) pole is 7.5°. These small angular offsets confirm that the MAX-phase and intermetallic phase share nearly identical pole directions along the sample normal.

Based on the crystallographic parameters of Cr_2AlC (hexagonal, a = 2.85 Å, c = 12.8 Å) and Al_4Cu_9 (approximated cubic lattice parameter a = 8.70 Å), an in-plane lattice matching analysis was performed. Along the proposed alignment direction $Cr_2AlC[100] \parallel Al_4Cu_9[001]$, three Cr_2AlC lattice repeats (3×2.85 Å = 8.55 Å) closely match one Al_4Cu_9 lattice repeat (8.70 Å).

The resulting linear lattice misfit of δ is calculated as follows:

$$\delta = \frac{|8.55 - 8.70|}{(8.55 + 8.70)/2} \times 100\% \approx 1.74\% \quad (1)$$

where the value of 1.74% indicates a low lattice mismatch between the two phases under the proposed orientation relationship.

2.2 | Electrical Contact Performance of the Coatings

After electrical contact testing, the arcing time, arc energy, and contact resistance were recorded, and their variations with contact counts are shown in Figure 3a,b. During the first 500 electrical contact cycles, all coated samples maintained low and stable contact resistance without significant breakdown, as depicted in Figure 3b. In contrast, the uncoated 7075 aluminum alloy exhibited pronounced fluctuations in contact resistance.

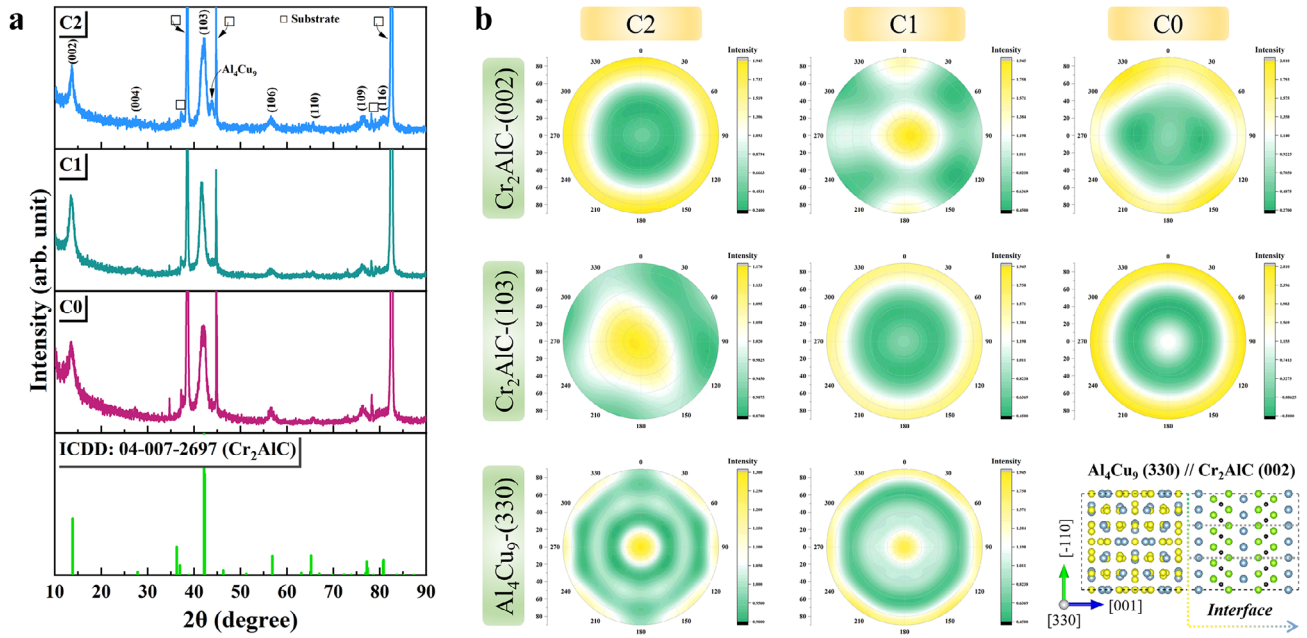

FIGURE 2 | (a) XRD patterns of the annealed coatings. (b) Pole figures of Cr_2AlC (002), Cr_2AlC (103) and Al_4Cu_9 (330) for all coatings.

Figure 3c further compares the resistance behavior of C0, C1, and C2 during the first 500 cycles. Among them, the C2 coating, with its low-resistance characteristics, exhibited the best welding resistance: both contact resistance and arcing time remained at low levels with minimal fluctuations, indicating excellent arc-extinguishing capability. However, during subsequent cycles, all coatings eventually failed due to breakdown, leading to a sharp increase in contact resistance.

After repeated cyclic electrical contact testing, resistive heating and arc discharge rapidly elevate the contact temperature, leading to the formation of localized molten pools. These pools spatter under the combined effects of electrostatic forces, electromagnetic forces, and surface tension. After arc extinction, the molten material solidifies quickly. As a result, each switching cycle produces a characteristic structure in which the arc center radiates outward, as shown in Figure S4a–d. The corresponding 3D morphologies of the electrical contact surfaces are also presented in Figure S4a–d.

The surface morphology of the coated samples exhibits a crater-like shape with splatter around the periphery, whereas the contact morphology of the uncoated aluminum alloy substrate shows a crater-like depression with a central protrusion. EDS mapping results indicate that a substantial amount of molten copper accumulates on the surface of the aluminum alloy substrate. In contrast, in the coating's arc ablation zone, a brittle, fracture-prone oxide phase containing copper, aluminum, and chromium is formed. Furthermore, when copper is incorporated into the coating, a highly conductive Al-Cu phase appears in the arc ablation region and disperses toward the edges.

The contact angles between different material pairs were obtained using the Owens-Wendt method. The measured contact angles and surface energies are listed in Table 1. The contact angle between Cu and C1 or C2 was below 80°, indicating that the wettability of Cu on Cr_2AlC-Cu coatings is acceptable. However, the contact angle between Cu and either the 7075 substrate or the C0 coating exceeded 87°, implying that the intrinsic bonding in these cases is insufficient to form a reliable contact.

Figure S4e shows the XRD patterns of the electrical contact surfaces, obtained using micro-XRD analysis. The results indicate that, after electrical contact testing, the phase composition on the aluminum substrate consists primarily of aluminum and copper. For the C0 and C1 samples, the contact surfaces contain not only aluminum and copper but also Cr_2AlC and Cr_7C_3 phases. Moreover, with a further increase in Cu content, the Al_4Cu_9 phase was also detected near the contact surface of the C2 sample. The localized transient flash temperatures at microscopic contact asperities were estimated using the classical Holm theory of electrical contacts [37]. The relevant equation is $\theta_f^2 - \theta_0^2 = U_c^2/(4L)$, where θ_f is the absolute flash temperature at the contact spot, θ_0 is the initial temperature of the sample (293 K), $U_c = I*R_s$ is the voltage drop across the microscopic contact spot, I = 3 A is the applied current, R_s is the contact resistance, and $L = 2.45 \times 10^{-8}\ V^2K^{-2}$ is the Lorenz constant. Based on the experimentally measured initial contact resistance of approximately 0.1-0.2 Ω under a current of 3 A, the corresponding flash temperatures were estimated to be approximately 729 and 1666°C, respectively. These values represent estimated localized transient peak temperatures rather than the bulk temperature of the coating. Such intense local flash heating could provide sufficient thermal activation for elemental redistribution and localized thermal decomposition of Cr_2AlC into Cr_7C_3 at highly concentrated current-carrying asperities, consistent with the Cr_2AlC-to-Cr_7C_3 decomposition observed at elevated temperatures in previous in situ TEM studies [38].

To further clarify the mechanism by which Cu doping affects the electrical contact properties of the coatings, the cross-sectional microstructures of the electrical contact regions in the C0 and C2

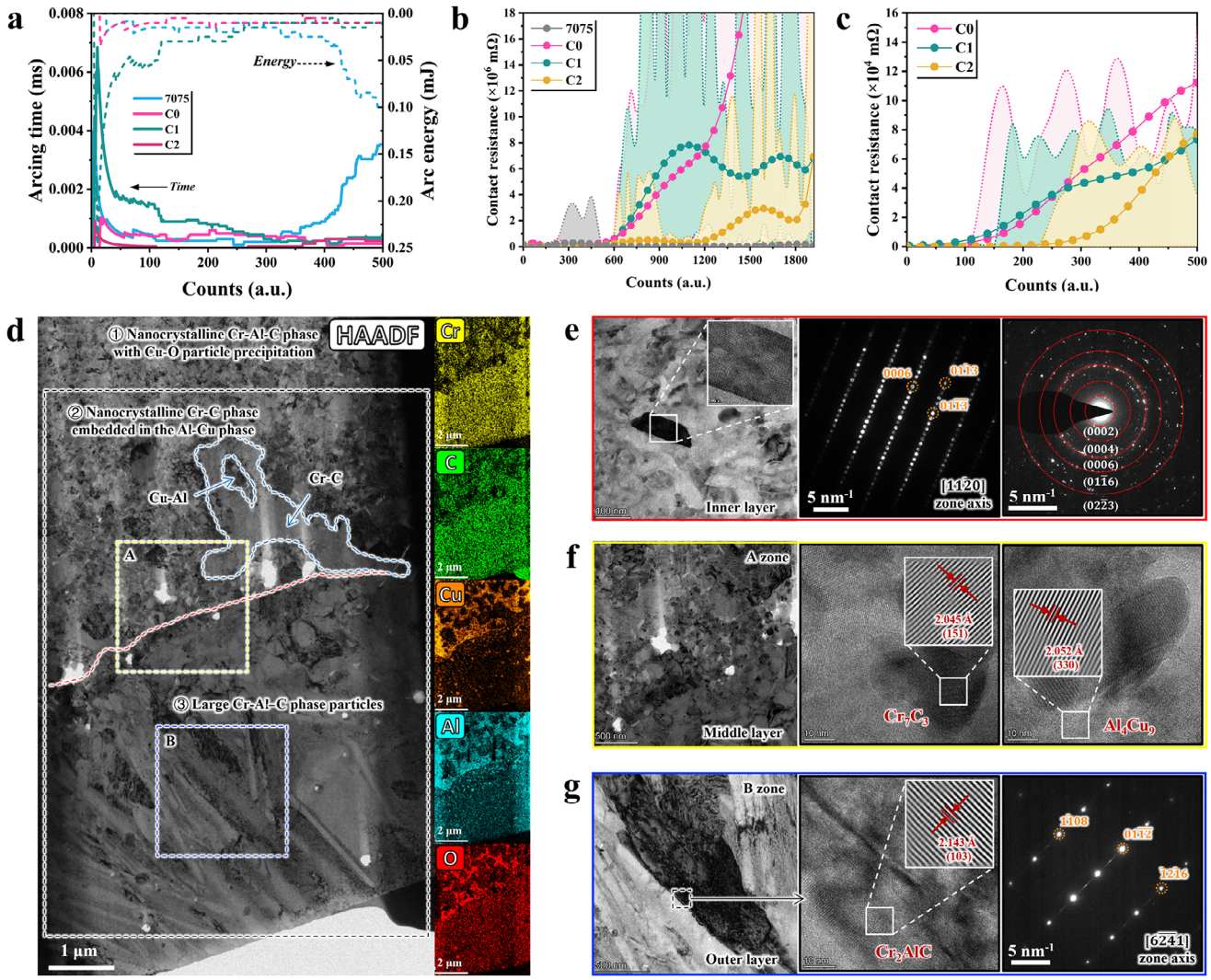

FIGURE 3 | (a) Arcing time, arc energy, and (b) contact resistance as a function of electrical contact counts for all coatings. (c) Variation in contact resistance of all coatings during 500 electrical contact cycles. (d) Cross-sectional HAADF image and corresponding EDS mapping results of the C2 sample. Enlarged views of the (e) inner layer, (f) middle layer (yellow dashed box), and (g) outer layer (blue dashed box) in (d), with corresponding SAED and FFT patterns.

TABLE 1 | Contact angles and surface energies between different interfaces.

Material combination	σ_s (N/m)	σ_l (N/m)	σ_{sl} (N/m)	Contact angle θ (°)
Cu on 7075	45.70	44.70	0.99	87.32
Cu on C0	45.70	46.79	0.99	87.43
Cu on C1	45.70	41.07	0.99	72.54
Cu on C2	45.70	49.59	0.99	72.18

samples were analyzed using TEM. The results are presented in Figure S5 and Figure 3d–g, respectively.

According to the EDS mapping results, Figure S5a shows that five distinct regions appear in the sample cross-section after cyclic electrical contact testing. From the interior of the coating to the surface, these regions are identified as: (1) raw coating, (2) heat-affected zone (HAZ), (3) nanocrystalline Cr-C phase embedded in the Al-Cu phase, (4) coarse Cr-C particles with Cu precipitation, and (5) a thin Al-Cu phase layer. Figure S5b–d present enlarged images of regions 2, 3, and 4, respectively. Figure S5b shows a bright-field TEM image of region 2, revealing coarse grains with nanocrystalline features. The interplanar spacing in the FFT image corresponding to the white-marked area was measured to be 0.214 nm, which corresponds to the (006) plane of the Cr_2AlC MAX phase. Based on this result, the hexagonal Cr_2AlC along the

[2111] zone axis was further indexed, where the $(10\bar{1}\bar{3})$, $(01\bar{1}0)$ and $(\bar{1}103)$ planes could be clearly identified. The enlarged image of the coating-substrate interface in Figure S5b also reveals a distinct multilayer structure, consistent with the annealed microstructure shown in Figure 1d. Figure S5c shows the bright-field TEM image of the upper region of the C0 coating. TEM analysis indicates that spherical copper particles are present within large Cr_7C_3 particles, while the top layer of the coating consists of an Al_4Cu_9 phase covering the surface of the larger Cr_7C_3 particles. Figure S5d presents the microstructure of the middle region of the coating, where nanocrystalline Cr_7C_3 phases are encapsulated by an amorphous Al-Cu mixture phase. In summary, after cyclic electrical contact testing, the heat generated during operation leads to: (i) the formation of an Al-Cu phase on the surface; (ii) thermal decomposition of the upper Cr_2AlC phase; (iii) formation of coarse Cr_7C_3 particles; (iv) generation of nanocrystalline Cr_7C_3 phases in the intermediate layer; (v) formation of an internal amorphous Al–Cu phase due to Cu diffusion; and (vi) growth of a high-purity Cr_2AlC phase in the innermost layer.

Compared with the C0 sample, the cross-sectional microstructure of the C2 sample, according to the EDS mapping results, can be divided into three regions: (1) nanocrystalline Cr-Al-C phase with Cu-O particle precipitation, (2) nanocrystalline Cr-C phase embedded in the Al-Cu phase, and (3) large Cr-Al-C particles, as shown in Figure 3d. Figure 3e–g show enlarged bright-field TEM images of the inner layer, middle layer, and outer layer, respectively. Based on the SAED pattern analysis, a nanocrystalline Cr_2AlC phase was identified near the substrate, with the hexagonal Cr_2AlC along the $[11\bar{2}0]$ zone axis further indexed. The crystal planes (0006), $(01\bar{1}3)$ and $(01\bar{1}\bar{3})$ were clearly identified. Analysis of interplanar spacings further distinguished nanocrystalline Cr_7C_3 and Al_4Cu_9 phases in the middle region of the coating, as shown in Figure 3f, indicating the coexistence of both phases. The interplanar spacing measured in the FFT TEM image in Figure 3g was 0.2143 nm, which corresponds well with the Cr_2AlC (103) plane. The hexagonal Cr_2AlC along the $[6\bar{2}\bar{4}1]$ zone axis was further indexed. Therefore, compared with the C0 sample, the C2 sample retained a relatively intact, conductive Cr_2AlC MAX phase structure in the coating after cyclic electrical contact testing. Unlike C0, its surface layer did not transform into the high-resistance Cr_7C_3 phase. Moreover, although Cr_7C_3 appeared in the central region of the coating, the presence of a low-resistance Al_4Cu_9 network meant that the overall conductivity of the coating remained less affected.

2.3 | Mechanical and Current-Carrying Tribological Properties of the Coatings

The hardness, Young's modulus, and their relative ratios are presented in Figure S6. The results show that adding copper to Cr-Al-C coatings has little effect on hardness, which ranges from 18.8 to 21.2 GPa. However, Young's modulus increases with copper addition. Consequently, the addition of copper raises Young's modulus while leaving hardness largely unchanged, resulting in lower H/E and H^3/E^2 ratios. These ratios represent the resistance to elastic deformation and the ability to dissipate energy during plastic deformation under loading, respectively. This indicates that Cr_2AlC-Cu coatings exhibit lower toughness than pure Cr_2AlC coatings.

Figure 4a,b show the surface morphology and elemental distribution of the wear tracks of the uncoated and C2 samples after current-carrying wear testing, while the corresponding results for the C0 and C1 coatings are provided in Figure S7a–f. Despite the relatively short total sliding distance of 3 m, the uncoated 7075 aluminum alloy exhibited substantial material loss and pronounced wear scars, indicative of severe adhesive wear. In contrast, all coated samples showed no discernible wear tracks, suggesting excellent resistance to current-carrying wear. EDS mapping revealed the presence of copper-rich debris adhered to the surfaces of the coated specimens, confirming that wear primarily occurred on the copper counterpart balls rather than the coatings themselves. Correspondingly, the post-test XRD patterns (Figure S7g) displayed characteristic diffraction peaks of Cu on the coated sample surfaces, further validating the EDS observations. The wear rate analysis quantitatively supports these findings. The uncoated aluminum alloy exhibited a high wear rate of $(4.82 \pm 0.26) \times 10^{-3}$ $mm^3 \cdot N^{-1} \cdot m^{-1}$, while the wear rates of the copper balls paired with the C0, C1, and C2 coatings were markedly lower: $(1.94 \pm 0.32) \times 10^{-4}$, $(3.56 \pm 0.55) \times 10^{-4}$, and $(4.13 \pm 0.60) \times 10^{-4}$ $mm^3 \cdot N^{-1} \cdot m^{-1}$, respectively. These values suggest that wear in the coated systems predominantly occurred on the softer copper counterbody rather than the coating itself. This shift in the frictional contact regime, from a coating-copper interface to a copper-copper sliding pair, resulted in a notably reduced coefficient of friction (~0.15), as shown in Figure 4c. By contrast, the uncoated aluminum substrate experienced severe adhesive wear against the copper ball, yielding a significantly higher friction coefficient (~0.35). As shown in Figure 4d, although the uncoated aluminum alloy initially exhibited a lower average contact resistance (approximately 75% of that measured for the coated samples), its resistance fluctuated sharply during testing. In contrast, the coated samples demonstrated highly stable contact resistance throughout the current-carrying wear process. This stability highlights the coatings' ability to maintain consistent electrical contact and mechanical integrity under combined electrical and tribological loading conditions.

Figure S8 shows the cross-sectional TEM images of the C0 coating after the current-carrying wear test. Based on EDS mapping and compositional analysis of different regions, the copper alloy layer adhering to the surface of the C0 sample consists of four distinct layers, as shown in Figure S8a. Figure S8b presents an enlarged view of the interface between the coating and the adherent layer, while Figure S8c further enlarges the region marked in Figure S8b, revealing a thin amorphous aluminum oxide layer between the coating and the adherent layer. The FFT atomic-resolution TEM image inserted in Figure S8c, marked with a blue dashed box, shows an interplanar spacing of 0.179 nm, which matches the Cu crystal plane. A coherent twin boundary, marked with a yellow dashed line, confirms the presence of nanotwinned copper. The SAED pattern in Figure S8d exhibits distinct diffraction rings, indicating nanocrystalline Cu and ZnO phases with multiple crystal planes coexisting in the inner layer of the adherent layer. In contrast, the SAED pattern in Figure S8e reveals nanocrystalline Cu-Zn alloy and Cu phases with various crystal planes coexisting in the outer layer. Overall, the adherent layer on the surface of the C0 sample consists of four zones, from inner to outer: a continuous amorphous aluminum oxide layer, a mixed zone of copper particles and zinc oxide, a copper-zinc oxide layer, and an outer copper-zinc alloy layer.

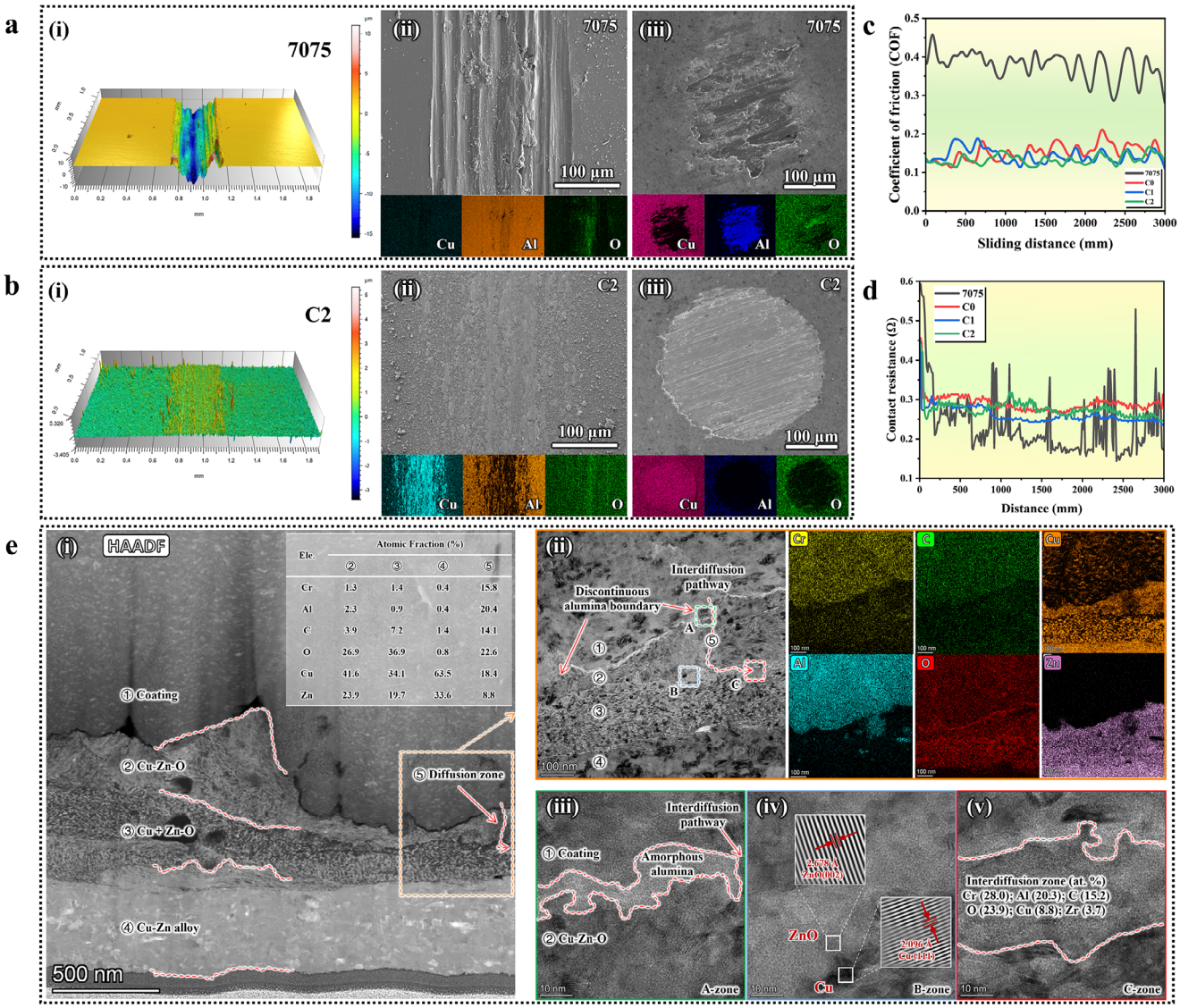

FIGURE 4 | 3D surface morphology and SEM images of current-carrying wear tracks for (a) the uncoated sample and (b) the C2 coating. (c) The coefficient of friction and (d) contact resistance of all coatings measured during the current-carrying wear test. (e) Cross-sectional TEM analysis of the C2 sample.

Figure 4e (i) shows the cross-sectional microstructure of the adherent layer on the surface of the C2 sample after the current-carrying test. Based on HAADF image contrast and compositional analysis, three distinct regions can be identified. Figure 4e (ii) provides an enlarged view of the orange dashed box in Figure 4e (i), while Figure 4e (iii, v) enlarge the green, blue, and red dashed boxes in Figure 4e (ii), respectively. The adhesion layer of the C2 sample shows a composition similar to that of the C0 sample and consists of a thin amorphous aluminum oxide layer, a Cu-Zn-O mixed zone, and an outer Cu-Zn alloy layer. Analysis of the FFT images in Figure 4e (iv) reveals interplanar spacings of 0.268 and 0.210 nm, corresponding to the (002) plane of ZnO and the (111) plane of Cu, respectively, confirming the coexistence of Cu and ZnO phases in the middle region of the adherent layer. Notably, the amorphous alumina layer between the coating and the adhesion layer is discontinuous, as shown in Figure 4e (iii). The detection of Al and Cr elements in the adhesion layer indicates diffusion from the coating, as evidenced by the EDS mapping results (Figure 4e (ii)) and compositional analysis (Figure 4e (v)), where the red dashed lines mark possible Al/Cr interdiffusion pathways.

3 | Discussion

3.1 | Cu-Assisted Crystallization Pathways of the Cr_2AlC MAX Phase

XRD patterns and microstructural characterization of the Cu-free C0 coating reveal only partial formation of the Cr_2AlC MAX phase, which is primarily attributed to the limited thermal budget provided by the low annealing temperature of 400°C. In contrast, Cu incorporation markedly promotes MAX-phase crystallization, as evidenced in Figure 1f. The originally alternating Cr-rich and Al-rich layers observed in the annealed C0 sample are disrupted,

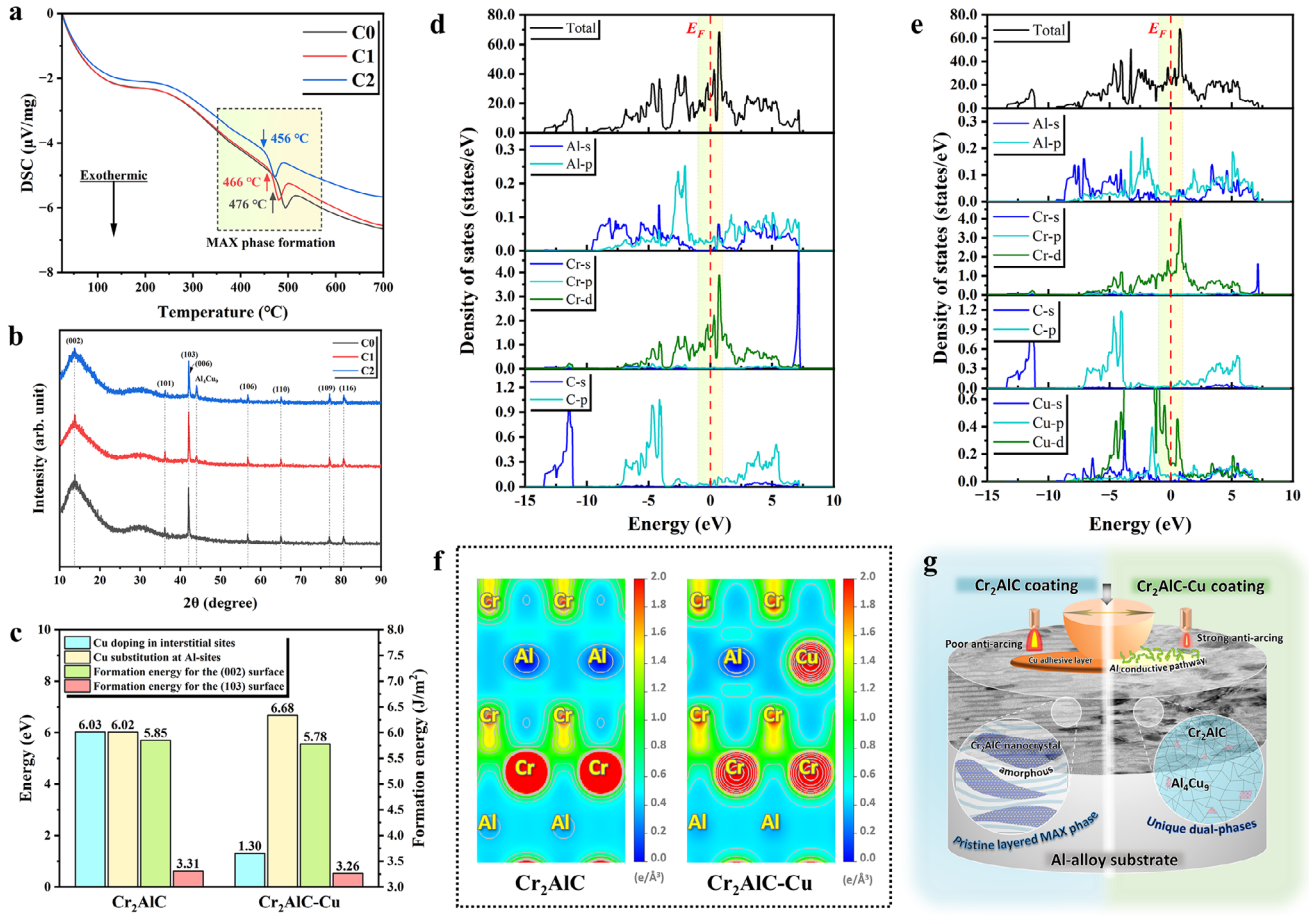

FIGURE 5 | (a) Differential scanning calorimetry (DSC) curves of the as-deposited coatings. (b) XRD patterns of post-tested samples. (c) Calculated Al vacancy formation energies and surface formation energies of Cr_2AlC with Cu incorporation. (d) Total and partial density of states (DOS) of pristine Cr_2AlC. (e) Total and partial density of states (DOS) of Cu-containing Cr_2AlC. (f) Electronic charge density maps of pristine and Cu-incorporated Cr_2AlC, illustrating the Cu-induced redistribution of local bonding characteristics. (g) Schematic illustration of the structural evolution of Cr_2AlC and Cr_2AlC-Cu coatings under electrical contact, highlighting the superior arc-erosion and current-carrying wear resistance of the Cu-doped coating.

and the amorphous diffraction rings in SAED patterns disappear upon Cu addition, indicating enhanced crystallinity.

To further elucidate the effect of Cu on the formation behavior of Cr_2AlC, DSC analysis was performed for all coatings (Figure 5a). The DSC curves exhibit a dominant exothermic event associated with crystallization, whose peak temperature systematically shifts with increasing Cu content. No Fe-containing phases were detected. These observations are fully consistent with the XRD and TEM results and demonstrate that Cu effectively lowers the crystallization barrier of the MAX phase.

It is worth noting that the crystallization of amorphous Cr_2AlC may involve metastable intermediate phases. Abdulkadhim et al. [39] reported the formation of a hexagonal $(Cr,Al)_2C_x$ phase prior to the development of the ordered Cr_2AlC MAX phase. In the present coatings, however, no distinct diffraction or SAED features could be unambiguously assigned to $(Cr,Al)_2C_x$. Moreover, DSC measurements reveal only one dominant exothermic event at approximately 450°C, suggesting that the crystallization-related processes may overlap within a narrow temperature range and cannot be clearly resolved into separate transformation steps. Thus, the possible transient formation of a $(Cr,Al)_2C_x$-like intermediate cannot be excluded, but its presence cannot be directly confirmed from the current results. Instead, our results indicate that Cu-assisted Al-Cu interdiffusion enhances atomic redistribution and accelerates the overall crystallization kinetics, facilitating the development of the Cr_2AlC MAX phase during prolonged annealing at 400°C.

TABLE 2 | Diffusion prefactor (D_0) and activation energy (Q) of Al and Cu atoms for solid-state diffusion in the Cu-Al binary system [41].

Metal	Diffusion element	D_0 (m^2/s)	Q (J/mol)
Al	Cu	8.4×10^{-5}	1.36×10^5
Cu	Al	4.8×10^{-6}	1.66×10^5

The acceleration of Cr_2AlC crystallization is closely associated with Cu-assisted Al-Cu interdiffusion. From a kinetic standpoint, the interdiffusion behavior is governed by the diffusion coefficients of Al and Cu, which follow the Arrhenius relation [40]. Using the diffusion parameters summarized in Table 2 [41], the diffusion coefficient of Cu in Al at 400°C (~2.3×10^{-15} m^2/s) is nearly four orders of magnitude higher than that of Al in

Cu (~6.8×10^{-19} m^2/s). This pronounced diffusion asymmetry significantly enhances atomic mobility on the Al side, leading to the accumulation of point defects, steep compositional gradients, and Cu segregation within Al-rich regions. The resulting Cu-rich nanocrystals act as effective heterogeneous nucleation sites, thereby increasing nucleation density, accelerating crystallization kinetics, and facilitating the rapid breakdown of amorphous bands.

Consistent with this mechanism, XRD patterns of the C2 coating (Figure 2a) reveal the formation of a substantial Al_4Cu_9 intermetallic phase, indicating the coexistence of Cr_2AlC and Al_4Cu_9. Among Al-Cu intermetallic compounds, Al_4Cu_9 possesses the most negative standard Gibbs free energy of formation [41], rendering it thermodynamically favorable. In combination with the nanocrystalline microstructure and nanoscale Al-Cu mixing in the C1 and C2 coatings, these conditions preferentially promote Al_4Cu_9 formation [42]. Importantly, Al_4Cu_9 exhibits a low electrical resistivity of 14.2 μΩ·cm [43], which contributes to the reduced resistivity observed in Cu-rich coatings.

Pole-figure analysis reveals a near coincidence of Cr_2AlC and Al_4Cu_9 pole positions in both low- and high-Cu samples, providing compelling evidence for an axial epitaxial relationship between the MAX phase and the intermetallic phase. The small angular deviations (2.5° and 7.5°) indicate that the corresponding crystallographic plane normals are nearly parallel, implying that Al_4Cu_9 precipitates adopt preferred orientations dictated by the Cr_2AlC matrix rather than forming randomly oriented grains. This axial epitaxy is particularly remarkable given the distinct crystallographic symmetries of the two phases, with Cr_2AlC exhibiting a layered hexagonal structure and Al_4Cu_9 approximated by a cubic lattice for translational matching.

The proposed orientation relationship of $(002)_{Cr_2AlC} \parallel (330)_{Al_4Cu_9}$, $[100]_{Cr_2AlC} \parallel [001]_{Al_4Cu_9}$ is strongly supported by the lattice matching analysis. A supercell configuration consisting of three Cr_2AlC a-lattice repeats matched to one Al_4Cu_9 lattice repeat yields a low misfit of 1.74%, which is sufficient to sustain semi-coherent interfaces. The corresponding misfit dislocation spacing of approximately 50 nm suggests that a large fraction of the interface remains elastically accommodated, thereby minimizing interfacial strain energy and conferring a kinetic growth advantage to epitaxially aligned Al_4Cu_9 grains.

This axial epitaxial coupling provides a mechanistic explanation for the non-monotonic texture evolution observed with increasing Cu content. At low Cu concentrations, a limited amount of Al_4Cu_9 promotes basal-plane alignment of Cr_2AlC without significantly impeding MAX-phase growth. At higher Cu concentrations, the increased Al_4Cu_9 volume fraction enhances the template effect, redistributing dominant Cr_2AlC orientations while preserving axial alignment between the two phases.

To clarify the intrinsic mechanism by which Cu modifies Cr_2AlC formation, first-principles calculations were conducted to evaluate the effect of Cu occupation on Al vacancy formation energy (Figure 5c). When Cu occupies interstitial sites, the Al vacancy formation energy is markedly reduced, indicating destabilization of local Al bonding and enhanced Al diffusivity. This reduction provides an atomic-scale explanation for the experimentally observed acceleration of MAX-phase crystallization and the lowered formation temperature. In contrast, substitutional Cu increases the Al vacancy formation energy, stabilizing the A layer and suppressing Al diffusion. Consequently, extensive substitutional solubility of Cu in Cr_2AlC is thermodynamically unfavorable, driving excess Cu to segregate and react with fast-diffusing Al to form Al-Cu intermetallic phases.

In addition to defect energetics, Cu incorporation also modifies surface stability. As shown in Figure 5c, Cu reduces the surface formation energies of both the (002) and (103) planes, with a more pronounced stabilization of the (002) plane at low Cu contents. Such differential stabilization of surface energetics provides a thermodynamic basis for the experimentally observed texture evolution, where (002)-oriented grains are favored under limited Cu incorporation. With further Cu addition, however, the growing prevalence of Al_4Cu_9 intermetallic phases progressively modifies the local growth environment, diminishing the dominance of surface energy minimization and enabling alternative orientations to become statistically competitive during film growth.

The electronic origin of Cu-induced stabilization in Cr_2AlC is further elucidated by density of states (DOS) analysis, as shown in Figure 5d. Pristine Cr_2AlC exhibits metallic characteristics, with the states near the Fermi level predominantly contributed by Cr-3d orbitals, while Al-p and C-p states play a minor role through hybridization. Upon substitutional incorporation of Cu at Al sites, additional Cu-d states emerge and strongly hybridize with Cr-3d states in the energy range from approximately -2 to 0 eV, indicating that Cu acts as an electronically active dopant rather than a rigid-band impurity. Importantly, the Cr-C framework remains largely unaffected, as reflected by the nearly unchanged C-p states, demonstrating that the structural backbone of the MAX phase is preserved.

These modifications in the electronic structure, particularly the enhanced hybridization between Cu-3d and Cr-3d states near the Fermi level, are expected to increase the density of states at the Fermi level and facilitate electron transport, thereby contributing to the improved electrical conductivity of the coating.

Electronic charge density maps (Figure 5f) provide complementary real-space insight into the local bonding modification induced by substitutional Cu. In pristine Cr_2AlC, charge density is strongly localized around Cr atoms and along Cr-C bonds, consistent with the covalent-dominant nature of the Cr-C slabs, whereas the Al layers exhibit more diffuse metallic bonding. Upon Cu substitution at Al sites, pronounced charge accumulation is observed around Cu atoms, accompanied by a redistribution of electron density in the neighboring Cr-Al coordination environment. This redistribution reflects strong Cu-Cr electronic interactions and the formation of more electronically saturated Cr-Cu bonds, which stabilize the A layer and increase the energetic cost of Al vacancy formation.

From an experimental perspective, Cu is predominantly present in the form of Al-Cu intermetallic phases, while a minor fraction may be incorporated into the Cr_2AlC lattice through substitution at Al sites due to the similar atomic size and electronegativity.

In addition, interstitial Cu may facilitate Al diffusion and contribute to Al_4Cu_9 formation.

In summary, these results support a dual-role scenario for Cu in Cr_2AlC: substitutional Cu stabilizes the A layer and suppresses Al diffusion through enhanced Cr-Cu bonding, whereas interstitial Cu, when present, is likely to lower the effective diffusion barrier by reducing the energetic cost of Al vacancy formation. This kinetically mediated competition between MAX-phase crystallization and Al-Cu intermetallic precipitation provides a consistent explanation for the experimentally observed dual-phase microstructure and texture evolution.

3.2 | Role of Cu in Electrical Transport and Arc-Erosion Stability of the Coatings

XRD and TEM results confirm that Cu addition promotes the formation of a well-crystallized Cr_2AlC MAX-phase microstructure together with a low-resistivity Al_4Cu_9 intermetallic phase. Additionally, modifications in the electronic structure are expected to enhance carrier transport, further contributing to the improved electrical conductivity. These combined effects largely account for the minimal electrical resistivity exhibited by the C2 coating. Electrical contact tests further demonstrate that C2 shows the shortest and most stable arcing time. Because resistive Joule heating is directly related to coating resistivity, the higher resistivity of the Cu-free C0 coating is expected to result in elevated cycling temperatures during electrical testing.

As shown in Figure S5, the C0 coating undergoes pronounced compositional gradients and structural stratification under the combined influence of Joule heating and arc heating. From the surface to the substrate, a distinct layered structure develops. In the surface layer, Al volatilization at high temperature [38] drives Cr-C phase restructuring, leading to the formation of Al-depleted regions and coarse Cr_7C_3 grains. In the subsurface layer, molten Cu permeation induces Al-Cu interdiffusion and the formation of Al-Cu intermetallic phases encapsulating underdeveloped nanocrystalline Cr_7C_3. In deeper regions, thermal conduction facilitates partial crystallization of the Cr_2AlC MAX phase, while the innermost layer retains a weakly crystallized structure due to insufficient heat transfer. This stratified evolution is primarily governed by localized overheating associated with steep thermal gradients, together with Cu melt penetration.

In contrast, the Cu-containing C2 coating evolves in a more uniform manner under electrical contact conditions, as shown in Figure 3d. Pre-doped Cu atoms undergo electrothermally driven interdiffusion with Al, enhancing atomic mobility and accelerating microstructural rearrangement. Owing to the lower resistivity of the C2 coating, Joule heating is effectively mitigated, which suppresses surface Al volatilization and enables the Cr_2AlC MAX phase near the surface to crystallize while maintaining structural integrity.

It is worth noting that the pre-existing Al_4Cu_9 phase should not be regarded as a direct diffusion barrier that physically prevents Al depletion from the MAX phase. Instead, its primary beneficial effect arises from its low electrical resistivity, which, together with the conductive Cr_2AlC MAX phase, facilitates more efficient current transport and reduces resistive Joule heating. The resulting reduction in local thermal exposure indirectly suppresses excessive Al volatilization and thermal decomposition of the near-surface Cr_2AlC, thereby contributing to the preservation of the MAX phase during electrical contact. Nevertheless, excessive formation of the relatively brittle Al_4Cu_9 phase may compromise the mechanical damage tolerance of the coating, as reflected by the reduced H/E and H^3/E^2 ratios with increasing Cu content (Figure S6). Therefore, Cu incorporation involves a trade-off between electrical and electrothermal benefits and mechanical damage tolerance, suggesting that an optimized Cu content, rather than excessive intermetallic formation, is critical for achieving balanced multifunctional performance.

In the subsurface region, Cu diffusion promotes Al-Cu intermetallic formation while simultaneously inducing the precipitation of nanocrystalline Cr-C phases, resulting in a composite structure consisting of Cr-C nanocrystals encapsulated by Al-Cu phases. At greater depths, thermal conduction supports the development of highly crystalline Cr_2AlC.

During electrical contact cycling, this accelerated crystallization of the MAX phase, together with the formation of an interconnected Al-Cu conductive network, enhances electrical conductivity and further suppresses Joule and arc heating, thereby establishing a positive feedback mechanism. Additionally, mechanical deformation induced by repeated contact and impact during electrical testing may contribute to localized energy dissipation and heating, thereby assisting grain growth. However, this effect is considered secondary compared to Joule heating. In addition, the Cu-induced evolution of the Cr_2AlC crystallographic texture contributes to a more distributed current transport pathway, which helps alleviate current localization under high electrical loads.

In summary, compared with the C0 coating, the C2 coating exhibits superior anti-welding behavior and more stable electrical contact performance. These improvements can be attributed to two key structural advantages. First, the presence of a highly crystalline Cr_2AlC MAX phase throughout the coating provides efficient metallic conduction pathways and avoids current blocking by high-resistivity Cr_7C_3 phases. Second, the incorporation of Cu enhances thermal conductivity, accelerates heat dissipation, mitigates localized overheating, and reduces arc initiation. Collectively, these factors endow the C2 coating with markedly improved electrical contact reliability.

3.3 | Cu-Modulated Current-Carrying Wear Mechanisms

In this study, a Cr_2AlC coating with a hardness of 21.2 GPa was successfully prepared via low-temperature annealing at 400°C, exceeding previously reported values [44]. This enhanced hardness is attributed to the refined microstructure and the coexistence of amorphous and nanocrystalline domains induced by low-temperature annealing. The C1 coating containing 3.9 at.% Cu exhibited a hardness comparable to that of the Cu-free C0 sample, which can be ascribed to Cu-induced grain refinement (Figure S2f). In contrast, the C2 coating with higher Cu content

displayed the lowest hardness (18.8 GPa), primarily due to the formation of the relatively soft Al_4Cu_9 intermetallic phase.

Current-carrying wear tests revealed pronounced differences in tribological behavior between the coated samples and the uncoated substrate. The uncoated 7075 aluminum alloy exhibited severe plowing pits after sliding, which can be attributed to localized temperature rise leading to Al melting. The molten aluminum adhered to the Cu counter-body, accelerating material removal and resulting in unstable friction behavior and fluctuating contact resistance.

In contrast, all coated samples developed a uniform adherent Cu layer on their surfaces after sliding. This behavior is attributed to the substantially higher hardness of the coatings (18.8-21.2 GPa) compared with pure Cu, which effectively transformed the tribological pair into a Cu-Cu contact system. The resulting Cu-Cu friction pair exhibited a low coefficient of friction of approximately 0.15 and facilitated the formation of a smooth and stable sliding interface, thereby ensuring consistent electrical contact and reduced wear. Notably, the presence of a crystallized MAX-phase matrix with a Cu-modulated texture further contributed to the stability of the contact interface by promoting distributed load support and current transport during sliding.

Interestingly, the wear rate of the Cu counter-body increased with increasing Cu content in the coatings. This trend is closely related to changes in surface energy and interfacial wettability between Cu and the coating. As summarized in Table 1, the contact angle of molten Cu on the coating surface decreases with increasing Cu doping, indicating enhanced interfacial affinity. Consequently, the C2 coating exhibits the highest surface energy with respect to Cu, facilitating stronger adhesion and retention of Cu during sliding, which leads to the formation of the thickest adherent Cu layer under current-carrying conditions.

It is worth emphasizing that the rapid establishment of this adherent Cu layer not only reduces the friction coefficient but also plays a crucial role in stabilizing the electrical contact interface by minimizing arc initiation during current-carrying operation. This adaptive interfacial evolution enables the coating surface to dynamically adjust to combined mechanical and electrical stimuli, thereby enhancing operational stability under severe service conditions.

Cross-sectional TEM analysis of the wear scars (Figure S8 and Figure 4e) further reveals fundamental differences between the C0 and C2 coatings after current-carrying wear. In the C0 coating, a continuous amorphous Al_2O_3 layer forms between the coating and the adherent Cu layer, acting as an insulating barrier that blocks direct electrical contact between the conductive MAX phase and the Cu counter-body, thus leading to elevated contact resistance. In contrast, in the C2 coating, Cu and Al within the coating mutually diffuse with Cu from the brass counter-body during sliding, disrupting the continuity of the alumina layer (Figure 4e (iii)). The localized rupture of this oxide film establishes direct metallic contact pathways composed of Al-Cu-Zn. Despite the presence of ZnO and other oxides within the adherent layer, these metallic pathways function as low-resistance conduction channels, significantly reducing the overall contact resistance once steady-state sliding is reached.

The exceptional current-carrying wear performance of the C2 coating can therefore be primarily attributed to Cu-assisted Al-Cu interdiffusion, which disrupts the insulating alumina layer and facilitates the formation of interconnected metallic conductive networks at the sliding interface. Within the adherent tribofilm, the emergence of oxygen-rich ZnO in intermediate regions is closely associated with its proximity to the frictional surface, where abundant environmental oxygen, frictional heating, and mechanical activation collectively accelerate selective oxidation of Zn. Owing to Zn's higher oxidation tendency compared with Cu, Zn preferentially oxidizes from the Cu-Zn alloy to form ZnO, while Cu segregates to generate localized metallic domains.

The coexistence of metallic Cu and ZnO phases reflects the coupled effects of selective oxidation, friction-induced nanocrystallization, localized thermal gradients, and dynamic tribological interactions. These processes collectively give rise to a self-organized, adaptive interfacial architecture that simultaneously stabilizes electrical conductivity and mechanical integrity during current-carrying operation. As schematically illustrated in Figure 5g, such self-adaptive structural evolution effectively suppresses arc erosion and mitigates wear, accounting for the superior durability and stable electrical contact behavior of the Cr_2AlC-Cu coating relative to the undoped Cr_2AlC counterpart.

4 | Conclusion

Cr_2AlC and Cu-doped Cr_2AlC coatings were successfully fabricated on 7075 aluminum alloy substrates using a hybrid arc–magnetron sputtering process followed by low-temperature annealing at 400°C. Cu incorporation markedly modifies the crystallization behavior and functional performance of the coatings. As the Cu content increases from 0 to 9.1 at.%, the microstructure evolves from a single Cr_2AlC MAX phase to a dual-phase system comprising Cr_2AlC and Al_4Cu_9 intermetallic phases. All coatings exhibit high hardness values (18.8-21.2 GPa), resulting from the combined effects of low-temperature-induced amorphous-nanocrystalline structures and Cu-assisted grain refinement.

Cu addition significantly reduces the electrical resistivity and enhances arc-erosion resistance, with the Cu-rich coating achieving the lowest resistivity of 119 μΩ·cm. This improvement originates from Cu-assisted Al-Cu interdiffusion and accelerated crystallization of the conductive MAX phase, which collectively establish efficient electrical pathways and suppress resistive heating under electrical contact conditions. During current-carrying sliding, the coatings promote the formation of an adherent Cu transfer layer, generating a stable Cu-Cu tribological interface with low friction and enhanced wear resistance. The coupled evolution of phase structure, electrical transport, and interfacial tribofilms constitutes a self-adaptive response to combined electrical, thermal, and mechanical stimuli.

Overall, this work demonstrates that Cu modification enables Cr_2AlC coatings to dynamically adapt their microstructure and interfacial state during service, providing a viable materials design strategy for advanced electrical contact systems requiring integrated conductivity, arc resistance, and tribological durability.

5 | Experimental

5.1 | Sample Fabrication

The Cr_2AlC-Cu coatings were deposited on 7075 aluminum alloy substrates using an arc-sputtering hybrid system. The aluminum alloy substrates with dimensions of φ 25.5 mm × 3 mm were prepared by wire cutting and subsequently polished with SiC paper followed by a diamond polishing agent. Before deposition, the substrates were ultrasonically cleaned progressively in acetone and ethanol each for 10 min, then blown dry with nitrogen gas. The cleaned substrates were immediately transferred into the deposition chamber. The chamber was evacuated to a base pressure of 4×10^{-3} Pa (3×10^{-5} Torr), while the substrates were heated to 400°C and maintained at this temperature throughout deposition.

Figure 1a presents a schematic of the deposition and heat-treatment systems for Cr-Al-Cu-C coatings. Chromium (Cr, 99.9% in purity) served as the arc target with a diameter of 128 and 8 mm in thickness. Two Al-Cu alloy targets (99.9% in purity, 400 × 100 × 7 mm) with atomic ratios of 90:10 and 80:20 were employed as sputtering targets to prepare coatings with different Cu contents. For Cr-Al-C coatings, pure aluminum (Al, 99.9% in purity) was used as the sputtering target. The target-substrate distance was fixed at 8 cm, and the substrate holder was rotated at 10 rpm.

Prior to deposition, the substrates were pretreated by Ar ion bombardment using a linear ion beam source (Ar flow: 35 sccm, 99.9995% purity) at a negative bias of 200 V for 30 min to remove surface oxides. During deposition, CH_4 gas (99.9995% purity) was introduced into the deposition chamber with a flow rate of 25 sccm, while the Ar flow rate was increased to 200 sccm. The working pressure was maintained at 2.7 Pa (2×10^{-2} Torr) by adjusting the gate valve between the chamber and the turbomolecular pump. The Al-Cu alloy or Al sputtering targets were operated at an average power of 3100 W, while the Cr target current was fixed at 60 A. A DC substrate bias of -150 V was applied for all depositions, which lasted 180 min.

After deposition, the coatings were annealed in a quartz-tube furnace evacuated to 3.0×10^{-4} Pa. The temperature was raised at 10°C/min to 400°C, held for 24 h, and then allowed to cool naturally to room temperature inside the furnace. Through this combined deposition and heat-treatment process, MAX-phase coatings were successfully obtained.

5.2 | Characterization of Specimens

The cross-sectional microstructure and chemical compositions of the Cr_2AlC-Cu coatings were examined using a field emission gun scanning electron microscope (FEG-SEM, Zeiss Sigma 300) equipped with an energy dispersive spectrometer (EDS, Oxford Instruments). The coating thickness was determined from cross-sectional SEM images by measuring more than nine randomly selected positions, and the average value was reported. The crystal structure and phase composition were analyzed by X-ray diffraction (XRD, D8 Advance DaVinci) with a Cu Kα1 source (λ = 1.5406 Å) operated at 40 kV × 40 mA. Conventional $\theta/2\theta$ scans were performed over a 2θ range of 10°-90°, with a step size of 0.02° and a scan rate of 4°/min. Raman spectroscopy (InVia Reflex, Renishaw) with a 532 nm laser was additionally employed to identify phase compositions. The surface morphology and roughness of the coatings were characterized using a 3D optical profilometer (UP-Lambda) equipped with a white-light interferometer (WLI). Measurements were performed at three randomly selected areas for each coating under identical conditions, and the average surface roughness (Sa) was reported.

The hardness and Young's modulus of the coatings were measured by nanoindentation using a nanoindenter equipped with a Berkovich diamond indenter. To minimize substrate effects, the maximum indentation depth was kept below 10% of the film thickness. A Poisson's ratio of 0.196 for Cr_2AlC, adopted from the literature [45], was used in the analysis. Ten measurements were conducted for each specimen, and the average values are reported.

The coating microstructure was further investigated by transmission-electron microscope (TEM, Talos F200x, Thermo Fisher) equipped with a high-angle annular dark-field (HAADF) detector. TEM specimens were prepared using a focused ion beam (FIB, Auriga, Carl Zeiss) with 2-30 kV Ga^+ ions. HAADF-STEM imaging was performed with an FEI Titan Chemi-STEM microscope fitted with a spherical aberration corrector (Cs-corrector). The instrument achieved a 0.1 nm probe size at a beam current of 70 pA and a convergence semi-angle of 19.8 mrad. Under a camera length of 135 nm, images were acquired using a HAADF detector with a collection angle range of 27.5-137.5 mrad.

The wettability of the MAX-phase coatings on 7075 aluminum and CuCrZr alloy substrates was evaluated using the Owens-Wendt method [46] with a contact angle measuring system (DCAT21). Before testing, all substrates were ultrasonically cleaned in acetone and methanol for 5 min each. Deionized water, ethylene glycol, 50% ethylene glycol, and glycerin were used as probe liquids. A 2 μL droplet was dispensed onto the surface using a micropipette, and contact angles were recorded. For each liquid, three measurements per specimen were taken, and the average values were used for analysis.

The current-carrying wear resistance of the coatings was tested with a pin-on-disk tribometer (TRB3) using an H62 copper ball (diameter: 6 mm) as the friction pair. Tests were performed at room temperature and ~30% relative humidity. A constant DC current of 3 A was applied between the sample and friction pair via a custom-made power loading assembly. The contact voltage during sliding was monitored with an oscilloscope. Linear sliding tests were performed with a load of 1 N, a sliding speed of 50 mm/s, and a stroke length of 5 mm. The total sliding distance was 3 m. For each coating, the current-carrying friction tests were repeated at least three times under identical conditions to ensure reproducibility, and the presented data represent typical results with negligible variation. Worn surfaces of both the coatings and friction pairs were examined by SEM in secondary electron imaging (SEI) mode. Compositional mapping of the wear tracks was performed by EDS, and 3D wear morphologies were further characterized by optical profilometry in WLI mode. The

wear rate (W) is calculated using the equation $W = \frac{S \times l}{N \times D}$, where S, l, N, and D are the cross-sectional area of the wear track, length of the wear track, loading, and total sliding distance, respectively.

The electrical resistivity of the coatings was measured using a four-point probe (Model 280 DI). Five measurements were taken in different directions for each specimen, and the average resistivity was reported. Electrical contact performance was evaluated with a JF04D electrical contact testing system. Coating samples ($10 \times 10 \times 3$ mm) served as cathodic static contacts, paired with a copper anode electrode at a 1 mm separation distance. The test conditions were: 24 V DC, 3 A constant current, 60 cycles/min contact frequency, and 40 cN contact force. A total of 1900 electrical contact cycles were performed. Contact resistance, arcing duration, and arcing energy were recorded throughout the tests.

The initial phase formation temperatures of MAX phase coatings with different copper contents were obtained using the differential scanning calorimetry (DSC) method with TG (STA 449 F3, Netzsch). The coatings were first deposited on the iron foil using the same methods and parameters as mentioned above, then subjected to delamination treatment to remove the substrate and isolate the coatings. Subsequently, the coatings were dried and ground to obtain corresponding coating powders. The alumina crucibles were utilized. The heat absorption/desorption curves of different coatings were recorded between 25°C and 700°C with a heating rate of 10°C/min. Nitrogen was employed as both the protective and purge gas.

5.3 | Atomic-Scale Calculations

First-principles calculations based on density functional theory (DFT) were carried out using the Vienna Ab initio Simulation Package (VASP) [47] in conjunction with the projector augmented-wave (PAW) method [48] to investigate the effect of Cu incorporation on the structural and electronic properties of Cr_2AlC. The exchange-correlation interaction was described within the generalized gradient approximation (GGA) using the Perdew-Burke-Ernzerhof (PBE) functional [49]. Brillouin zone integrations were performed using the Monkhorst-Pack method [50], with a k-point spacing of 0.02 $Å^{-1}$.

To model Cu incorporation, a $2 \times 2 \times 1$ Cr_2AlC supercell containing 32 atoms was constructed, in which Cu atoms were introduced at substitutional Al sites to represent dilute Cu doping. This substitutional configuration was selected due to its structural stability and relevance to equilibrium solid-solution behavior. During structural optimization, the lattice parameters and cell volume were fixed, while all atomic positions were fully relaxed until the total energy and atomic forces converged to 1×10^{-6} eV $atom^{-1}$ and 0.001 eV $Å^{-1}$, respectively. Since the constituent elements (Cr, Al, C, and Cu) of the studied system do not exhibit strong long-range magnetic ordering in the Cr_2AlC MAX phase under the conditions considered herein, magnetic effects were omitted. Therefore, spin polarization was not included in the calculations.

Author Contributions

Yiqun Feng: conceptualization, methodology, investigation, writing – original. **Qizhen He**: formal analysis, writing – original. **Guanshui Ma**: validation, investigation. **Zhenyu Wang**: writing – review & editing, data curation, supervision. **Peiling Ke**: methodology, investigation, funding acquisition. **Aiying Wang**: conceptualization, project administration, writing – review & editing, funding acquisition, supervision.

Acknowledgements

This work was financially supported by the National Key R&D Program of China (2024YFB3816500), the National Science Fund for Distinguished Young Scholars of China (52025014), National Natural Science Foundation of China (U22A20111), and Natural Science Foundation of Zhejiang Province (LR26E010004). Y. Q. Feng would like to thank Dr. Yuxi Xu for his valuable discussion on the figure modification.

Conflicts of Interest

The authors declare no conflicts of interest.

Data Availability Statement

The data that support the findings of this study are available from the corresponding author upon reasonable request.

References

1. I. Hwang, M. Seong, H. Yi, et al., "Low-Resistant Electrical and Robust Mechanical Contacts of Self-Attachable Flexible Transparent Electrodes With Patternable Circuits," *Advanced Functional Materials* 30 (2020): 2000458, https://doi.org/10.1002/adfm.202000458.

2. Y. Kim, Y. Jin, G. Yoon, et al., "Electrical Characteristics and Detailed Interfacial Structures of Ag/Ni Metallization on Polycrystalline Thermoelectric SnSe," *Journal of Materials Science & Technology* 35 (2019): 711–718, https://doi.org/10.1016/j.jmst.2018.11.020.

3. J. Song and V. Schinow, "Correlation Between Friction and Wear Properties and Electrical Performance of Silver Coated Electrical Connectors," *Wear* 330 (2015): 400–405, https://doi.org/10.1016/j.wear.2015.02.026.

4. N. D. Cox, C. D. Cress, J. E. Rossi, et al., "Modification of Silver/Single-wall Carbon Nanotube Electrical Contact Interfaces via Ion Irradiation," *ACS Applied Materials & Interfaces* 9 (2017): 7406–7411, https://doi.org/10.1021/acsami.6b14041.

5. A. B. Peters, D. Zhang, S. Chen, et al., "Materials Design for Hypersonics," *Nature Communications* 15 (2024): 3328, https://doi.org/10.1038/s41467-024-46753-3.

6. I. Dowding and C. A. Schuh, "Metals Strengthen With Increasing Temperature at Extreme Strain Rates," *Nature* 630 (2024): 91–95, https://doi.org/10.1038/s41586-024-07420-1.

7. J. Crespo-Miguel, S. Lucarini, A. Arias, and D. Garcia-Gonzalez, "Thermo-Electro-Mechanical Microstructural Interdependences in Conductive Thermoplastics," *npj Computational Materials* 9 (2023): 134.

8. A. E. Kheifets, I. V. Khomskaya, L. G. Korshunov, V. I. Zel'dovich, and N. Y. Frolova, "Effect of High Strain-Rate Deformation and Aging Temperature on the Evolution of Structure, Microhardness, and Wear Resistance of Low-Alloyed Cu-Cr-Zr Alloy," *Physics of Metals and Metallography* 119 (2018): 402–411, https://doi.org/10.1134/S0031918X18040075.

9. H. Fu, S. Xu, W. Li, J. Xie, H. Zhao, and Z. Pan, "Effect of Rolling and Aging Processes on Microstructure and Properties of Cu-Cr-Zr Alloy," *Materials Science and Engineering: A* 700 (2017): 107–115, https://doi.org/10.1016/j.msea.2017.05.114.

10. J. P. Barber, D. P. Bauer, K. Jamison, J. V. Parker, F. Stefani, and A. Zielinski, "A Survey of Armature Transition Mechanisms," *IEEE Transac-*

tions on Magnetics 39 (2003): 47–51, https://doi.org/10.1109/TMAG.2002.805913.

11. F. Stefani and R. Merrill, "Experiments to Measure Melt-wave Erosion in Railgun Armatures," *IEEE Transactions on Magnetics* 39 (2003): 188–192, https://doi.org/10.1109/TMAG.2002.805955.

12. X. Zhao, J. Ding, D. Xiao, L. Huang, and W. Liu, "Atomic-scale Investigation on the Evolution of T_1 Precipitates in an Aged Al-Cu-Li-Mg-Ag Alloy," *Journal of Materials Science & Technology* 209 (2025): 139–148, https://doi.org/10.1016/j.jmst.2024.04.073.

13. L. Lu, Y. Shen, X. Chen, L. Qian, and K. Lu, "Ultrahigh Strength and High Electrical Conductivity in Copper," *Science* 304 (2004): 422–426, https://doi.org/10.1126/science.1092905.

14. Z. Castro-Dettmer, R. M. Gee, and C. Persad, "Post-Test Characterization of a Chromium-Plated Copper Conductor," *Materials Characterization* 43 (1999): 251–258, https://doi.org/10.1016/S1044-5803(99)00011-X.

15. W. Lv, T. S. Chen, K. Q. Zheng, and Z. G. Zhang, "Feasible Preparation and Improved Properties of Ag-Graphite Composite Coating for Switch Contact by Cyanide-Free Electrodeposition," *Materials and Corrosion* 69 (2018): 933–940, https://doi.org/10.1002/maco.201709872.

16. P. D. Aalto and F. Y. Yee, "Plated Armature Contacts for Solid Armature Electromagnetic Railgun Launchers," *IEEE Transactions on Magnetics* 31 (1995): 667–672, https://doi.org/10.1109/20.364614.

17. T. G. Engel and N. M. Rada, "Time- and Frequency-Domain Characterization of Railgun Sliding Contact Noise," *IEEE Transactions on Plasma Science* 45 (2017): 1321–1326, https://doi.org/10.1109/TPS.2017.2705172.

18. I. L. Singer, M. J. Veracka, C. N. Boyer, and J. M. Neri, "Wear Behavior of Lubricant-Conditioned Copper Rails and Armatures in a Railgun," *IEEE Transactions on Plasma Science* 39 (2011): 138–143, https://doi.org/10.1109/TPS.2010.2062540.

19. X. Guo, X. Chen, P. Liu, et al., "Preparation and Mechanical Properties of Copper Matrix Composites Reinforced by Carbon Nanotubes and Al_2O_3," *Advanced Engineering Materials* 23 (2021): 2001490, https://doi.org/10.1002/adem.202001490.

20. G. Ma, A. Zhang, Z. Wang, et al., "MAX Phase Coatings: Synthesis, Protective Performance, and Functional Characteristics," *Materials Horizons* 12 (2025): 1689.

21. Z. Li, Z. Wang, G. Ma, et al., "High-Performance Cr2AlC MAX Phase Coatings for ATF Application: Interface Design and Oxidation Mechanism," *Corrosion Communications* 13 (2024): 27.

22. X. Li, X. Xie, J. Gonzalez-Julian, R. Yang, R. Schwaiger, and J. Malzbender, "Oxidation and Creep Behavior of Textured Ti_2AlC and Ti_3AlC_2," *Journal of the European Ceramic Society* 42 (2022): 364–375, https://doi.org/10.1016/j.jeurceramsoc.2021.10.018.

23. W. Tian, P. Wang, G. Zhang, Y. Kan, Y. Li, and D. Yan, "Synthesis and Thermal and Electrical Properties of Bulk Cr_2AlC," *Scripta Materialia* 54 (2006): 841–846, https://doi.org/10.1016/j.scriptamat.2005.11.009.

24. V. Desai, A. Shrivastava, A. B. Zala, T. Parekh, S. Gupta, and N. I. Jamnapara, "Manufacturing of High Purity Cr_2AlC MAX Phase Material and Its Characterization," *Journal of Materials Engineering and Performance* 33 (2024): 9841–9849, https://doi.org/10.1007/s11665-024-09513-4.

25. Z. J. Lin, M. S. Li, J. Y. Wang, and Y. C. Zhou, "High-Temperature Oxidation and Hot Corrosion of Cr_2AlC," *Acta Materialia* 55 (2007): 6182.

26. X. Chen, B. Stelzer, M. Hans, R. Iskandar, J. Mayer, and J. M. Schneider, "Enhancing the High Temperature Oxidation Behavior of Cr_2AlC Coatings by Reducing Grain Boundary Nanoporosity," *Materials Research Letters* 9 (2021): 127–133, https://doi.org/10.1080/21663831.2020.1854358.

27. A. Reuban, I. Povstugar, M. Rasiński, et al., "Unveiling the Diffusion Pathways Under High-temperature Oxidation of Cr_2AlC MAX Phase via Nanoscale Analysis," *Corrosion Science* 235 (2024): 112179, https://doi.org/10.1016/j.corsci.2024.112179.

28. T. L. Ngai, W. Zheng, and Y. Li, "Effect of Sintering Temperature on the Preparation of Cu-Ti_3SiC_2 Metal Matrix Composite," *Progress in Natural Science: Materials International* 23 (2013): 70.

29. D. Yang, Y. Zhou, X. Yan, H. Wang, and X. Zhou, "Highly Conductive Wear Resistant Cu/Ti_3SiC_2(TiC/SiC) co-continuous Composites via Vacuum Infiltration Process," *Journal of Advanced Ceramics* 9 (2020): 83–93, https://doi.org/10.1007/s40145-019-0350-4.

30. J. T. Wright, K. Forsythe, J. Hutchins, and R. W. Meulenberg, "Implications of Orbital Hybridization on the Electronic Properties of Doped Quantum Dots: The Case of Cu:CdSe," *Nanoscale* 8 (2016): 9417–9424, https://doi.org/10.1039/C6NR00494F.

31. L. Shao, W. Li, Q. Lu, et al., "Bonding Mechanism in Cu Coating Deposited on Al Alloy Substrate: Combining Molecular Dynamics Simulation and Experiment," *Materials Science and Engineering: A* 942 (2025): 148703, https://doi.org/10.1016/j.msea.2025.148703.

32. D.-Y. Wu, X. Zhou, L.-P. Li, et al., "Tuning the Microstructure, Mechanical Properties, Tribological and Electrical Contact Behavior by Cu Doping for Gold-based Coating," *Tribology International* 191 (2024): 109193, https://doi.org/10.1016/j.triboint.2023.109193.

33. H. S. Myung, H. M. Lee, L. R. Shaginyan, and J. G. Han, "Microstructure and Mechanical Properties of Cu Doped TiN Superhard Nanocomposite Coatings," *Surface and Coatings Technology* 163 (2003): 591–596, https://doi.org/10.1016/S0257-8972(02)00627-8.

34. B. Dong, X. Zhang, S. Cao, et al., "A Dual-bioinspired Laminated Approach Enables High Thermal Conductivity and Superior Toughness in Zero-thermal-expansion Copper Composites," *Acta Materialia* 304 (2026): 121799, https://doi.org/10.1016/j.actamat.2025.121799.

35. Y.-J. Jang, J.-I. Kim, J. W. Jang, M.-J. Jung, S.-H. Kwon, and J. Kim, "Effects of Mo-N-Cu Doping on Microstructural, Mechanical, and Tribological Properties of Thick ta-C Coatings for Cryogenic Applications," *Materials & Design* 260 (2025): 114990, https://doi.org/10.1016/j.matdes.2025.114990.

36. G. S. Fox-Rabinovich, K. Yamamoto, M. H. Aguirre, et al., "Multi-Functional Nano-Multilayered AlTiN/Cu PVD Coating for Machining of Inconel 718 Superalloy," *Surface and Coatings Technology* 204 (2010): 2465–2471, https://doi.org/10.1016/j.surfcoat.2010.01.024.

37. R. Holm, ed., *Electric Contacts: Theory and Applications*, Fourth Ed (Springer Science & B Media, 2013).

38. G. Ma, H. Wu, Z. Fang, et al., "Phase Formation Mechanism of Cr_2AlC MAX Phase Coating: In-situ TEM Characterization and Atomic-scale Calculations," *Journal of Materials Science & Technology* 206 (2025): 176–184, https://doi.org/10.1016/j.jmst.2024.03.037.

39. A. Abdulkadhim, M. Baben, T. Takahashi, et al., "Crystallization kinetics of amorphous Cr2AlC thin films," *Surface and Coatings Technology* 206 (2011): 599.

40. Y. Tanaka, M. Kajihara, and Y. Watanabe, "Growth Behavior of Compound Layers During Reactive Diffusion Between Solid Cu and Liquid Al," *Materials Science and Engineering: A* 6 (2007): 355–363, https://doi.org/10.1016/j.msea.2006.09.047.

41. J. Zhang, B. Wang, G. Chen, et al., "Formation and Growth of Cu-Al IMCs and Their Effect on Electrical Property of Electroplated Cu/Al Laminar Composites," *Transactions of Nonferrous Metals Society of China* 26 (2016): 3283.

42. R. Besson, M.-N. Avettand-Fènoël, L. Thuinet, et al., "Mechanisms of Formation of Al_4Cu_9 During Mechanical Alloying: An Experimental Study," *Acta Materialia* 87 (2015): 216–224, https://doi.org/10.1016/j.actamat.2014.12.050.

43. J. A. Rayne, M. P. Shearer, and C. L. Bauer, "Investigation of Interfacial Reactions in Thin Film Couples of Aluminum and Copper by Measurement of Low Temperature Contact Resistance," *Thin Solid Films* 65 (1980): 381–391, https://doi.org/10.1016/0040-6090(80)90248-5.

44. S. Zhou, J. Yuan, H. Wu, et al., "A Straightforward 3D Polycrystal Plasticity Finite Element Method for Dynamic/Static Recrystallization

Simulation," *Journal of Materials Science & Technology* 232 (2025): 180–198, https://doi.org/10.1016/j.jmst.2024.09.005.

45. J. Zhang, K. Tao, L. Ma, Y. Yang, L. Yang, and W. Duan, "First Principles Study on Structure and Mechanical Properties of Cr_2AlC," *AIP Advances* 12 (2022): 055019, https://doi.org/10.1063/5.0091402.

46. D. K. Owens and R. C. Wendt, "Estimation of the Surface Free Energy of Polymers," *Journal of Applied Polymer Science* 13 (1969): 1741.

47. G. Kresse and J. Furthmüller, "Efficient Iterative Schemes for Ab Initio Total-Energy Calculations Using a Plane-Wave Basis Set," *Physical Review B* 54 (1996): 11169–11186, https://doi.org/10.1103/PhysRevB.54.11169.

48. P. E. Blöchl, "Projector Augmented-Wave Method," *Physical Review B* 50 (1994): 17953.

49. J. P. Perdew, K. Burke, and M. Ernzerhof, "Generalized Gradient Approximation Made Simple," *Physical Review Letters* 77 (1996): 3865–3868, https://doi.org/10.1103/PhysRevLett.77.3865.

50. H. J. Monkhorst and J. D. Pack, "Special Points for Brillouin-Zone Integrations," *Physical Review B* 13 (1976): 5188–5192, https://doi.org/10.1103/PhysRevB.13.5188.

Supporting Information

Additional supporting information can be found online in the Supporting Information section.

Supporting File: adfm78286-sup-0001-SuppMat1.docx.